https://doi.org/10.5194/egusphere-2026-131
Preprint. Discussion started: 19 January 2026

Uncertainty estimation of aerosol properties from a Vaisala CT25k ceilometer based on in situ aerosol measurements

Marcus G. Müller[1], Birger Bohn[1], and Ulrich Löhnert[1,2]

[1]Forschungszentrum Jülich GmbH, Institute of Climate and Energy Systems: Troposphere (ICE-3), Jülich, Germany
[2]Institute for Geophysics and Meteorology, University of Cologne, Germany

Correspondence: Marcus G. Müller (marc.mueller@fz-juelich.de)

Abstract. In recent years, the use of automatic lidars and ceilometers (ALC) for atmospheric research has increased. Originally, these instruments were developed to measure cloud base height automatically, utilising the LIDAR principle. However, multiple studies have shown their usability for aerosol remote sensing and planetary boundary layer height detection. It is not only possible to calibrate a ceilometer and derive the attenuated backscatter signal, but also to retrieve aerosol extinction coefficients and aerosol mass concentrations by means of estimated extinction to mass coefficients (EMC). The ACTRIS national facility JOYCE (Jülich Observatory for Cloud Evolution) offers a multiyear dataset of cloud remote sensing measurements and ceilometer observations. So far, a method for measuring aerosol properties has been missing to use this dataset to quantify aerosol-cloud interaction. The goal of this study is to evaluate the applicability of a ceilometer aerosol retrieval to prove the value of this dataset for aerosol remote sensing. We present the workflow, starting with the raw ceilometer data, followed by a calibration of the backscatter coefficient profiles and a retrieval of aerosol properties. To evaluate the result of this workflow for the JOYCE ceilometer (Vaisala CT25k), in situ aerosol measurements at the Jülich meteorological tower were performed, where an optical particle sizer (OPS) was installed at 120 m above ground. Aerosol extinction coefficients σ_a were retrieved from the ceilometer attenuated backscatter signal with σ_a correlated with the in situ total aerosol mass concentration with R = 0.73. For our measurement set-up, aerosol mass concentrations can be derived from the retrieved σ_a with a mean absolute percentage error of 39 %. However, the extinction to mass conversion factor EMC = (2.2 $\pm$ 0.9) m^2g^{-1} derived from the measurements for a wavelength of 906 nm was found to be greater by a factor of about 1.8 compared to literature and to EMC calculated from Mie simulations based on the in situ aerosol size distributions. The mismatch is tentatively attributed to the limited aerosol size range of the OPS.

1 Introduction

Measuring and understanding the role of aerosols in the atmosphere is an essential part of modern atmospheric research. Aerosols in the atmospheric boundary layer determine the air quality relevant to human health (Russell and Brunekreef, 2009). Aerosols are also key ingredients for cloud formation and influence the global radiation budget directly and indirectly. Aerosol cloud interaction (ACI) creates the largest uncertainty in the estimation of anthropogenic radiative forcing (IPCC, 2021). The change of cloud albedo by a change in aerosol concentration is already well known (1st indirect effect, Twomey (1977)). Also,

https://doi.org/10.5194/egusphere-2026-131
Preprint. Discussion started: 19 January 2026

the effect of aerosols on cloud lifetime (2nd indirect effect, Albrecht (1989)) and the heating-caused cloud-burnoffs (semi-direct effect, Ackerman et al. (2000)) was identified. Still, there is a high need for collocated aerosol and cloud observations to quantify these effects.

Aerosol measurements can be performed in situ or with remote-sensing instruments. In many cities, urban air pollution is continuously monitored. Apart from trace gases (e.g. O_3, SO_2, NO_2), aerosol mass concentrations are typically measured as PM1, PM2.5 or PM10, comprising particle fractions with diameters below 1, 2.5 and 10 μm. These measurements are often located close to the emission sources and are mostly situated close to ground level. However, to quantify the effects of aerosols on the radiation budget and also on ACI, information about the vertical and spatial aerosol distribution is required. This information can be delivered by satellite observations (Quaas et al., 2006) covering large areas, however, with limited information under cloudy conditions, especially below clouds. Collocated cloud microphysical and below-cloud aerosol observations are therefore essential to quantify the effect of surface-originated aerosol on low-level clouds.

To observe aerosol concentration below clouds, ground-based lidar systems are suitable. There are several high-power lidar systems in Europe. A large fraction of these systems in Europe are included in the EARLINET network (D'Amico et al., 2015). This network will soon be integrated into the ACTRIS network (Pappalardo, 2018; Laj et al., 2024). These lidars all deliver precise measurements of aerosol extinction with a high temporal and vertical resolution. Due to the technical and financial demands for running these systems, the total number of installed instruments is currently limited to 27 (TROPOS, 2025), representing only a few regions. Additionally, these systems are mostly operated manually for selected periods, which limits the temporal coverage. These limitations can be tackled by the increasing number of ceilometers in Europe. Ceilometers could provide aerosol proxies below cloud base. It was shown that a combination of ceilometer, cloud radar and microwave radiometer can provide ACI parameters for low-level clouds by means of ground-based remote sensing (Sarna and Russchenberg (2016)). Today, a large network (486 stations in E-Profile, (E-Profile, 2025)) of automatic (low-power) lidars and ceilometers (ALC) already exists. These simple lidar systems, originally developed to measure cloud base height automatically, offer long-term datasets of atmospheric vertical backscatter profiles. It was shown that already the attenuated backscatter from a ceilometer correlates with the PM10 aerosol mass concentration (Münkel et al., 2006). Retrieval approaches have been developed to derive aerosol extinction coefficients and aerosol mass concentration from ceilometer backscatter. These retrievals are less accurate than those from a high-power lidar, mostly because of the reduced emission power and the single wavelength design of ALCs. Nonetheless, the combination of recently developed tools (Haefele et al., 2016; Hopkin et al., 2019; Mortier, 2022) already provides automated aerosol profile retrievals and can be applied to basically all existing ceilometer datasets.

This study aims to quantify the uncertainty of using an existing multi-year ceilometer dataset to derive aerosol properties. These are primarily aerosol extinction coefficients σ_a, to represent the optical aerosol properties, and aerosol mass concentrations, calculated from σ_a, as a common measure of aerosol load. An aerosol retrieval was applied for a ceilometer (Vaisala CT25k) of the Jülich Observatory for Cloud Evolution (JOYCE, Löhnert et al. (2015)). This observational site in the western part of Germany is an ACTRIS national facility, specialised in cloud remote sensing. To determine the uncertainty of the aerosol retrieval an in situ measurement for aerosol concentration was installed on top of an adjacent tower in 120 m height above ground. The comparison between in situ and remote-sensing measurements is presented in this study.

https://doi.org/10.5194/egusphere-2026-131
Preprint. Discussion started: 19 January 2026

This publication is split into four parts. In the second section, we shortly introduce the measurement site JOYCE, describe its geographical location and characterize the type of expected aerosols. In Sec. 3, we introduce the instruments used. In the fourth section, the methodology of calibrating the ceilometer and deriving aerosol extinction coefficients is presented. In Sec. 5, the measured in situ dataset is introduced, the potential of the ceilometer aerosol retrieval is illustrated for a case study and the uncertainties of the aerosol properties, i.e. attenuated backscatter, aerosol extinction coefficient and aerosol mass concentration, are determined based on a 6-month in situ aerosol measurement period from the tower.

2 Observational site

JOYCE is an atmospheric observatory in the western part of Germany (50.91 N, 6.41 E). It is a cooperative research initiative between the University of Cologne and Forschungszentrum Jülich (FZJ) (Löhnert et al., 2015). The observational platform is located at FZJ on the roof of a 20 m tall building in a more rural area, close to the cities Cologne and Aachen. Two open pit coal mines (Hambach in the east and Inden in the southwest) are within a 5 km distance. Also, two coal power plants are in close proximity, about 10 km southwest and 20 km northeast. The aerosol composition at FZJ was analyzed during the Jülich Atmospheric Chemistry Project (JULIAC) campaign in 2019 where submicron aerosols were sampled at a small tower in 50 m. It was shown with a high-resolution time-of-flight aerosolmass spectrometer (HR-ToF-AMS), that organic compounds contributed 40% to 60% of the total aerosol mass (Liu et al., 2024) of non-refractory submicron particles.

https://doi.org/10.5194/egusphere-2026-131
Preprint. Discussion started: 19 January 2026

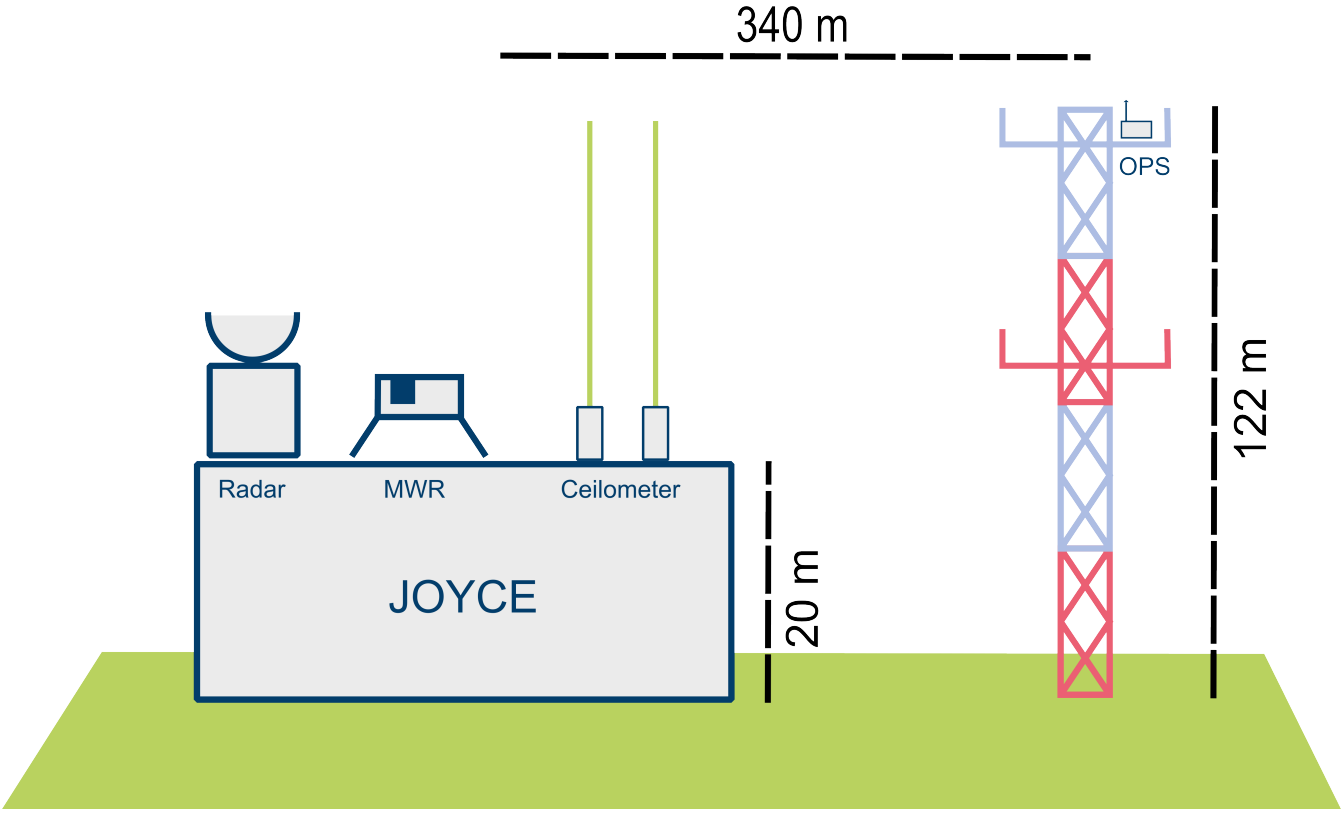

Figure 1. Not true-to-scale schematic of the experimental setup showing distances of the meteorological tower hosting the optical particle sizer (OPS) to the JOYCE-site with two ceilometers, a cloud radar and a microwave radiometer (MWR) at Forschungszentrum Jülich.

JOYCE is equipped with a suite of remote sensing, in situ and radiation measurement instruments. These instruments are among others an ABB Atmospheric Emitted Radiance Interferometer (AERI), a Metek MIRA-36 Doppler cloud radar, two ceilometers (Vaisala CT25k, Lufft CHM15k, Sec. 3.1), a RPG humidity and temperature profiler and a CIMEL sun photometer. The JOYCE data repository offers 16 years of ceilometer data. Additionally, a 120 m meteorological tower is located closeby. This tower provides standard meteorological measurements at seven platforms (10 m, 20 m, 30 m, 50 m, 80 m, 100 m and 120 m). The tower has a horizontal distance of 340 m from the JOYCE site. For this study, the tower was equipped with an optical particle sizer (OPS) (TSI OPS 3330) as an in situ instrument for comparison with the ceilometer aerosol retrievals. A scheme of the setup is shown in Fig. 1.

https://doi.org/10.5194/egusphere-2026-131
Preprint. Discussion started: 19 January 2026

3 Instrumentation

3.1 Ceilometers

Ceilometers are basic near-infrared lidar systems. They emit eye-safe laser pulses with a high frequency. The pulses are then scattered back to the instrument by cloud droplets, aerosols and gas-phase constituents. From the run-time, the distance to the scattering target is estimated. The intensity of the scattered signal can be used to determine the optical properties of the scattering target. The measured power P at the ceilometer receiver as a function of range r and time t can be described by the following equation (Hervo et al., 2016):

$$P(r,t) = \frac{1}{r^2} C_L(t) O(r,t) \beta(r,t) e^{-2\int_0^r \sigma(r',t)dr'} + B(t) \tag{1}$$

Here C_L represents a calibration factor (also known as lidar-constant), which contains device-specific parameters. The signal is also dependent on the overlap function $O(r,t)$, the extinction coefficient σ, the backscatter coefficient β and a solar background signal $B(t)$. It is common to define the range corrected signal (RCS) as:

$$RCS = (P(r,t) - B(t))\, r^2 \tag{2}$$

Each ceilometer generates manufacturer-dependent raw data that were brought to unified L1 data by the E-Profile algorithm Raw2L1 (Haefele et al., 2016).

JOYCE is equipped with two ceilometers representing the two main types of ceilometers, namely monoaxial (CT25k) and biaxial (CHM15k) setups. Monoaxial systems use a single light path for emitting and receiving the laser pulses and a semi-transparent mirror to split the beam. In contrast, biaxial ceilometers use two separate light paths. The downside of this approach is a range with incomplete overlap, which affects measurements of the CHM15k in the lowest about 350 m (Schween et al., 2014). This problem does not occur for the Vaisala CT25k, which covers the lowest range gate but has a significantly lower pulse energy. The Lufft CHM15k uses an avalanche photon detector (APD) in photon-counting mode, which allows higher SNR at high altitudes, compared to photocurrent method instruments like the Vaisala CT25k (Schween et al., 2014). It should also be noted that the CT25k and the CHM15k by now have been operational since 16 years and 12 years, respectively, which may have lowered their sensitivity. More advanced, modern ceilometers can produce data of higher quality. However, the intention of this work is to utilize the existing long-term dataset, which requires a characterization of the available instruments. The comparison with the in situ tower measurements will be confined to the CT25k data because of the overlap issue of the CHM15k at 120 m.

https://doi.org/10.5194/egusphere-2026-131
Preprint. Discussion started: 19 January 2026

Table 1. Ceilometers at JOYCE (based on manufacturer information)

	CT25k	CHM15k
Wavelength / nm	905	1064
Pulse energy / μJ	1.6	8
Pulse repetition rate / kHz	5.6	5-7
Range resolution / m	15	15
Temporal resolution / s	15	15
Min. measurement height / m	0	5[a]
Max. measurement height / m	7500	15000

[a] Reliable aerosol information starting around 350 m, due to limited overlap at lower altitudes (Schween et al., 2014)

3.2 Optical Particle Sizer

To evaluate the ceilometer aerosol-retrieval, a comparison setup was created as shown in Fig. 1 using the meteorological tower with an OPS for in situ measurements of aerosols installed at 120 m above ground. At this altitude, a representative measurement can be made undisturbed by any small-scale influence from the ground or nearby buildings.

The instrument consists of an inlet connected to the OPS in a water-tight box allowing for an omnidirectional aerosol sampling and rain protection (Eckert, 2013). It does not filter out any particles larger than 10 μm. A photograph of the setup is shown in panel (a) of Fig. 2. The airflow through the inlet of about 15 standard liter per minute (slm) was driven by a pump and controlled by a mass flow controller (MFC). Inside the laminar airflow about 1 slm of air was taken by the OPS instrument. The airflow of the MFC was regulated in a way that an isokinetic sampling by the OPS from the main airflow was obtained (assuming laminar flow conditions). A schematic of the sampling and OPS setup is illustrated in panel (b) of in Fig. 2. Specifications of the OPS can be found in Table 2.

Table 2. Manufacturer specifications of the optical particle sizer TSI OPS 3330

Size resolution	$<$5% at 0.5 μm
Size range	0.3 – 10 μm (in up to 16 channels)
Concentration range	0 – 3000 particles/cm^{-3}

The instrument works on the principle of light scattering as illustrated in Fig. 2. The inlet air flow (1 l/min) is focused by a sheath air stream and goes through a light trap where a continuous laser beam (660 nm) passes the particle stream. Scattered light from a range of scattering angles is focused on a photodetector by a mirror. Light scattered by single aerosol particels is registered and assigned to a particle size dependent on the scattered light intensity.

https://doi.org/10.5194/egusphere-2026-131
Preprint. Discussion started: 19 January 2026

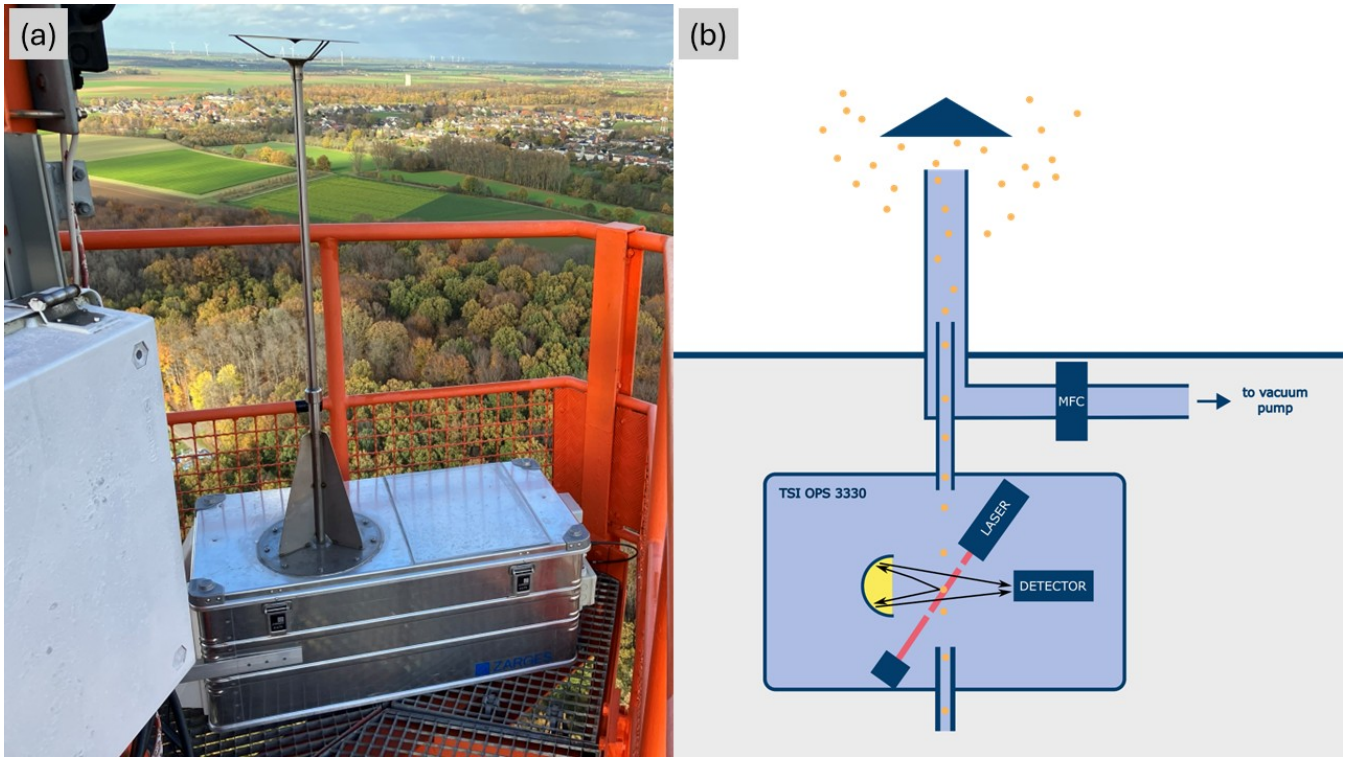

Figure 2. (a) Photograph of the in situ aerosol tower measurement setup at 120 m. (b) Schematic of the instrument consisting of a rain-protected inlet with sampling line, a pump-driven mass flow controller (MFC) and a TSI OPS 3300 for optical particle detection.

The system allows the measurement of aerosol mass and number concentrations, sorted in 16 user-defined size channels, based on their scattering intensity. According to the manufacturer, data are processed as follows. For each channel, the number concentration C_n in a bin is determined. Based on the number concentration, a mass concentration C_m can be estimated:

$$C_m = C_n \, \rho \, \frac{\pi D_{pv}^3}{6} \tag{3}$$

ρ is the particle density (typically in the range 1.2 to 2.5 cm^{-3} (Osborne et al., 2024)) taken as 1.5 g cm^{-3} and D_{pv} is an effective particle diameter, which is calculated from the bin upper boundary (D_U) and bin lower boundary (D_L):

$$D_{pv} = D_L[\frac{1}{4}(1+(\frac{D_U}{D_L})^2)(1+(\frac{D_U}{D_L}))]^{\frac{1}{3}} \tag{4}$$

Size bins were selected based on a predefined protocol (TSI Default) as summarised in Tab. A1 in the Appendix to cover the range 0.3 - 10 μm. Moreover, a temporal resolution of 5 min and a sample time of 1 min were selected for the measurements.

3.3 Cloudnet

The Cloudnet target classification (Hogan and O'Connor, 2004) is utilized to characterize the atmospheric boundary layer regarding the presence of aerosols, insects, clouds and precipitation. Cloudnet was founded to combine ground based cloud

https://doi.org/10.5194/egusphere-2026-131
Preprint. Discussion started: 19 January 2026

remote sensing instruments to a network and to generate synergistic products (Illingworth et al., 2007). The minimum instrumentation consists of a Doppler cloud radar, a ceilometer and a dual-frequency microwave radiometer. Today, Cloudnet is integrated into the center for cloud remote sensing (CCRES) within ACTRIS (Pappalardo, 2018; Laj et al., 2024). Currently there are 29 contributing sites registered (Cloudnet, 2025). The Cloudnet target classification combines radar reflectivity, ceilometer backscatter, model parameters, microwave radiometer LWP measurements and rain gauge measurements into a single classification product. For each height layer, the bit values can be set for presence of small liquid droplets, presence of falling hydrometeors, wet-bulb temperature below 0 °C, presence of melting ice particles, presence of aerosols and presence of insects. At JOYCE, the Cloudnet target classification is available on a grid of 36 m vertical resolution and 30 s temporal resolution. In the following, it will be used to filter out conditions where remote aerosol detection by the ceilometers may be adversely affected by liquid clouds, ice clouds or precipitation.

4 Ceilometer Aerosol Retrieval

4.1 Calibration Verification

To use the RCS of a ceilometer for aerosol measurements, a calibration of the signal is necessary. The goal of this calibration is to determine the lidar constant C_L to convert the RCS (Eq. 2) into an attenuated backscatter coefficient β_{att}.

$$\beta_{\mathrm{att}} = \frac{\mathrm{RCS}}{C_L} \tag{5}$$

The commonly used Rayleigh calibration (Wiegner and Geiß, 2012) could not be applied to the Vaisala CT25k ceilometer due to the low signal-to-noise ratio (SNR) in high altitudes for this instrument. In recent years, an additional method was established. The liquid cloud calibration (Hopkin et al., 2019; O'Connor et al., 2004) uses the attenuation of the ceilometer signal in liquid clouds. The lidar ratio S, defined as the ratio of the extinction-to-backscatter coefficient is assumed to be constant inside liquid clouds with a value of $S \approx 18$ sr (Pinnick et al., 1983; O'Connor et al., 2004). For cases where the ceilometer signal is fully attenuated by a liquid cloud, the total path integrated attenuated backscatter B can be described as a function of the observed attenuated backscatter coefficient β_{att}, the height above ground z, the range corrected signal RCS, the multiple-scattering correction η, the lidar ratio and a calibration coefficient C (Hopkin et al., 2019):

$$B = \int_0^\infty \beta_{\mathrm{att}}\, dz = \int_0^\infty C\,\mathrm{RCS}\, dz = \frac{1}{2\eta S} \tag{6}$$

In the algorithm, the calibration coefficient C is varied until $B\eta$ = 0.0266 m^{-1}. This value represents liquid cloud droplets with S = 18.8 sr (Hopkin et al., 2019). Only profiles with a negligible aerosol backscatter contribution (< 5%) below the cloud are considered. The optimised calibration coefficient C is the reciprocal of the lidar constant C_L. This method does not require high SNR values in high tropospheric regions and so it can be applied also to avalanche photon detectors in photocurrent detection mode like the Vaisala CT25k.

https://doi.org/10.5194/egusphere-2026-131
Preprint. Discussion started: 19 January 2026

The JOYCE CT25k already performs an internal calibration, which was verified by the liquid cloud calibration (Hopkin et al., 2019), based on the program code of E-Profile (Haefele et al., 2016). A lidar constant of $C_L = 0.97 \pm 0.06$ was determined in the years 2023 and 2024, confirming the internal calibration of the instrument. The manufacturer does not disclose the nature of the internal calibration.

4.2 Aerosol Extinction Profiles

To derive extinction profiles from the ceilometer attenuated backscatter signal the Klett-Fernald-Sasano method (Klett, 1981, 1985) is mostly used where a backward inversion approach is applied to solve the lidar equation. The calculations start in the high, aerosol-free part of the atmosphere (Rayleigh-atmosphere) and iteratively derive the extinction coefficients.
To use the Klett-Fernald-Sasano approach, a high SNR in high layers is necessary. This requirement can not be fulfilled when using a Vaisala CT25k ceilometer. For this reason, a forward method was used (Li et al., 2021). For each layer z_i, starting at the ground with initial conditions based on the β_{att}, the aerosol transmittance T_a, the molecular transmittance T_m, the aerosol backscatter coefficient β_a and the molecular backscatter coefficient β_m are calculated in an iterative process (k = 1, 2, 3...). The values of $T_m(z_i)$ and $\beta_m(z_i)$ were calculated from the station altitude based on an algorithm-specific Rayleigh atmosphere. Here τ_a represents the aerosol optical depth and σ_a the aerosol extinction coefficient.

$$\tau_a(z_i, k) = \tau_a(z_{i-1}) + \sigma_a(z_i, k-1) \cdot \Delta z_i \tag{7}$$

$$T_a^2(z_i, k) = e^{-2\tau_a(z_i, k)} \tag{8}$$

$$\beta_a(z_i, k) = \frac{\beta_{\text{att}}(z_i)}{T_m^2(z_i) \cdot T_a^2(z_i, k)} - \beta_m(z_i) \tag{9}$$

At every iteration step k, the extinction coefficient σ_a is calculated with the lidar ratio S_a:

$$\sigma_a(z_i, k) = S_a \cdot \beta_a(z_i, k) \tag{10}$$

The iterative process is stopped if either 30 iteration steps are reached or if the relative change of the extinction coefficient σ_a is smaller than 0.01%. Then the current value of σ_a, τ_a and β_a are set and the process starts for the next layer. This method was implemented in the Python-library A-Profiles (Mortier, 2022). For this study, we used this forward inversion algorithm for the Vaisala CT25k ceilometer.

The lidar ratio $S_a = \sigma_a / \beta_a$ is unknown for ceilometer measurements. Therefore, it was estimated based on a multi-year mean value of $S_a = (47 \pm 13)$ sr for a wavelength of 1020 nm from the AERONET (AErosol RObotic NETwork, Holben et al. (1998)) inversion product of a CIMEL sun photometer installed next to the ceilometers. The uncertainty of S_a is a major contributor to the overall uncertainty of retrieving σ_a from a ceilometer with this method.

https://doi.org/10.5194/egusphere-2026-131
Preprint. Discussion started: 19 January 2026

4.3 Calculation of aerosol mass concentration

Aerosol mass concentration C_m can be calculated from the aerosol extinction coefficient σ_a by an extinction to mass coefficient (EMC):

$$C_m = \frac{\sigma_a}{\mathrm{EMC}} \tag{11}$$

The EMC is dependent on the aerosol type, size distribution and the ceilometer wavelength. The EMC can either be predicted theoretically by Mie simulations (Mortier, 2022) or determined based on in situ C_m and ceilometer-derived σ_a. A discussion of the experimental EMC values found in this study compared to literature values can be found in section 5.3.

5 Results and Discussion

The results section is split into five subsections. At first, an overview of the in situ and ceilometer datasets is given and data from an example day are presented. Afterwards, the quality of retrieving aerosol mass concentrations from ceilometer backscatter coefficients and ceilometer aerosol extinction coefficients is evaluated. Finally, an attempt is presented to reproduce aerosol backscatter and extinction coefficients based on the measured size distributions, followed by a critical assessment of the OPS measurements.

5.1 Dataset overview and example day

A dataset of ceilometer-derived attenuated backscatter coefficients in 120 m and of in situ aerosol mass concentrations in the same height was acquired for the period 01 February to 20 June 2023. There was a 10-day interruption from 22 February to 03 March because of a blocked exhaust filter and a 7-day interruption from 04 April to 12 April caused by an outage in ceilometer measurements. The dataset was screened to avoid contamination by hydrometeors in the ceilometer signal, based on the Cloudnet target classification (Sec. 3.3). To further refine this selection, data were discarded when the relative humidity (RH) measured at 120 m exceeded 95 % and cloud radar reflectivity at the lowest possible measurement height (255 m) was above -20 dBZ at 35 GHz.

https://doi.org/10.5194/egusphere-2026-131
Preprint. Discussion started: 19 January 2026

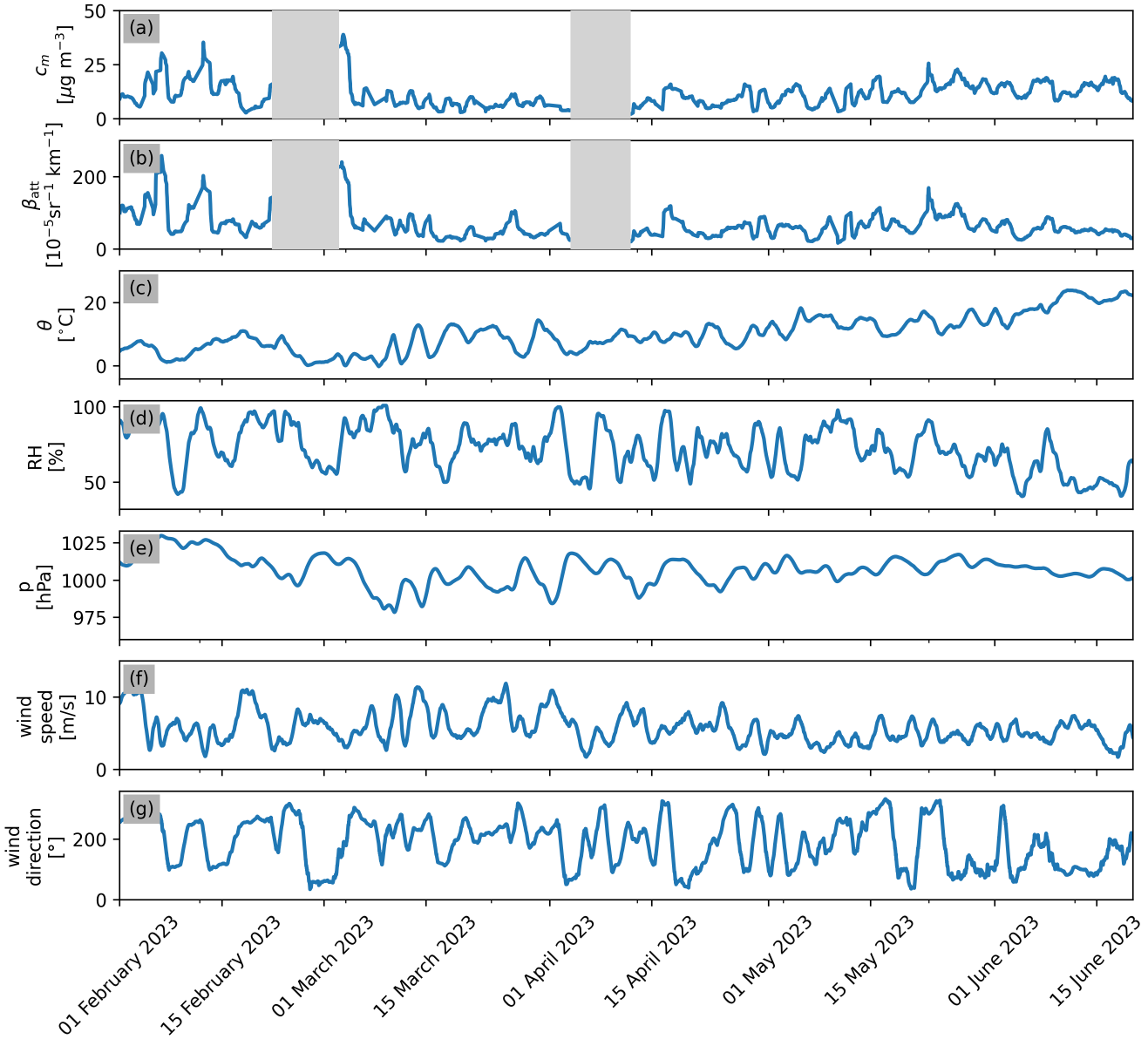

Figure 3. Atmospheric conditions during the measurement period from 01 February to 20 June 2023 with (a) OPS in situ aerosol mass concentration C_{m} at 120 m, (b) ceilometer attenuated backscatter signal β_{att} at 120 m and further in situ data: (c) temperature θ at 120 m, (d) humidity RH at 120 m, (e) ground air pressure p, (f) wind speed at 120 m, and (g) wind direction at 50 m. All data are shown as 1-day rolling means. C_{m} and β_{att} were filtered based on the criteria specified in Sect. 5.1.

Figure 3 provides an overview of the dataset, including additional measurements from the meteorological tower. The mean aerosol mass concentration during the observation period was C_{m}= 11.5 μg m^{-3}. The mean temperature and relative humidity

https://doi.org/10.5194/egusphere-2026-131
Preprint. Discussion started: 19 January 2026

were θ = (12 ± 7) °C and RH = (76 ± 19) %, respectively. The wind speed at 120 m above ground on average was (6 ± 3) m s^{-1}. For the measurement period, no coherent wind direction measurement in 120 m was available. For this reason, the wind direction at the meteorological tower 50 m above ground is shown in Fig. 3. The predominant wind direction at 50 m was
220 west-southwest.

To illustrate typical diurnal changes in aerosol concentration, 14 February 2023 was selected as an example. This day was dominated by a high-pressure ridge over Central Europe. The ridge went along with a surface high-pressure system. This situation creates stable conditions with no clouds or precipitation over the day.

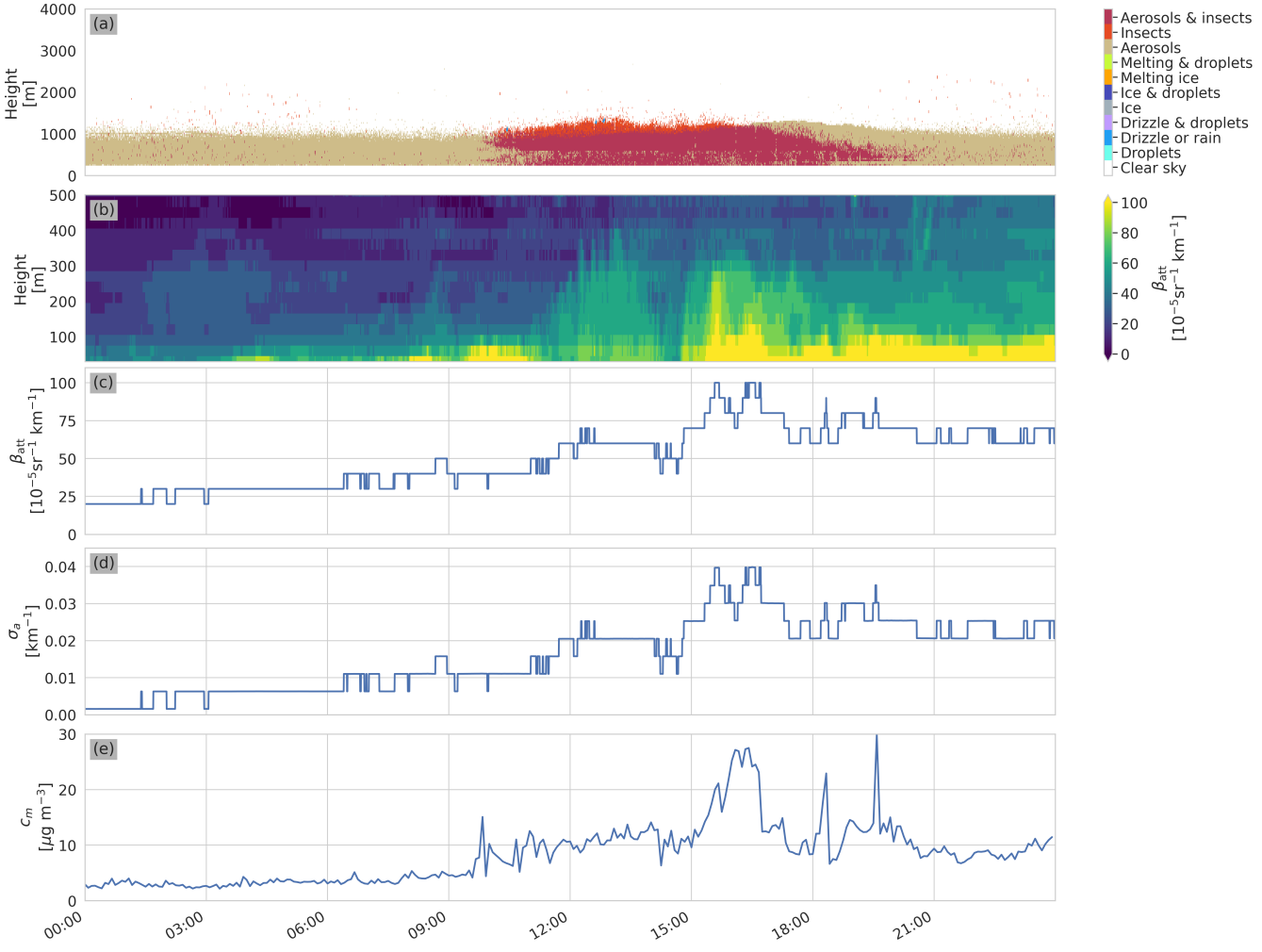

Figure 4. One day case study from 14 February 2023 in Jülich, showing (a) the Cloudnet target classifications, (b) ceilometer attenuated backscatter coefficients β_{att}, (c) ceilometer attenuated backscatter coefficients β_{att} at 120 m, (d) ceilometer-derived aerosol extinction coefficients σ_a at 120 m and (e) in situ aerosol mass concentration C_m at 120 m.

https://doi.org/10.5194/egusphere-2026-131
Preprint. Discussion started: 19 January 2026

As shown in panel (a) of Fig. 4, the Cloudnet target classification confirmed no clouds or precipitation in the boundary layer while aerosols were present for the whole day. These conditions make that day ideal for comparing the ceilometer aerosol retrieval with the in situ observation. In the time range from 0:00 to about 8:00 low aerosol mass concentrations of $C_{\mathrm{m}} < 5$ μg m^{-3} are visible in the tower observations (panel (e)). This goes along with low ceilometer backscatter coefficients of $\beta_{\mathrm{att}} < 40 \times 10^{-5}\mathrm{sr}^{-1}\mathrm{km}^{-1}$ (panel (c)). The vertical extent of the aerosol layer below 250 m is visible in the ceilometer backscatter profiles (panel (b)). With the development of the mixing layer after 9:00, the aerosol mass concentration increased up to C_m = 30 μg m^{-3}. This trend is also visible in the ceilometer-derived aerosol extinction coefficients (panel (d)) and in the ceilometer backscatter coefficients, which increased up to β_{att} = $100\times10^{-5}\mathrm{sr}^{-1}\mathrm{km}^{-1}$ (panel (c)).

This example demonstrates qualitativly that ceilometer backscatter coefficients can reproduce the overall change in aerosol concentration. Steplike levels of ceilometer backscatter coefficients can be explained by the low signal resolution of the Vaisala CT25k (Sect. 3.1).

5.2 Aerosol mass concentration and attenuated backscatter coefficient

In the next step, we now statistically relate measured attenuated backscatter coefficients β_{att} to in situ measured aerosol mass concentrations C_{m}.

https://doi.org/10.5194/egusphere-2026-131
Preprint. Discussion started: 19 January 2026

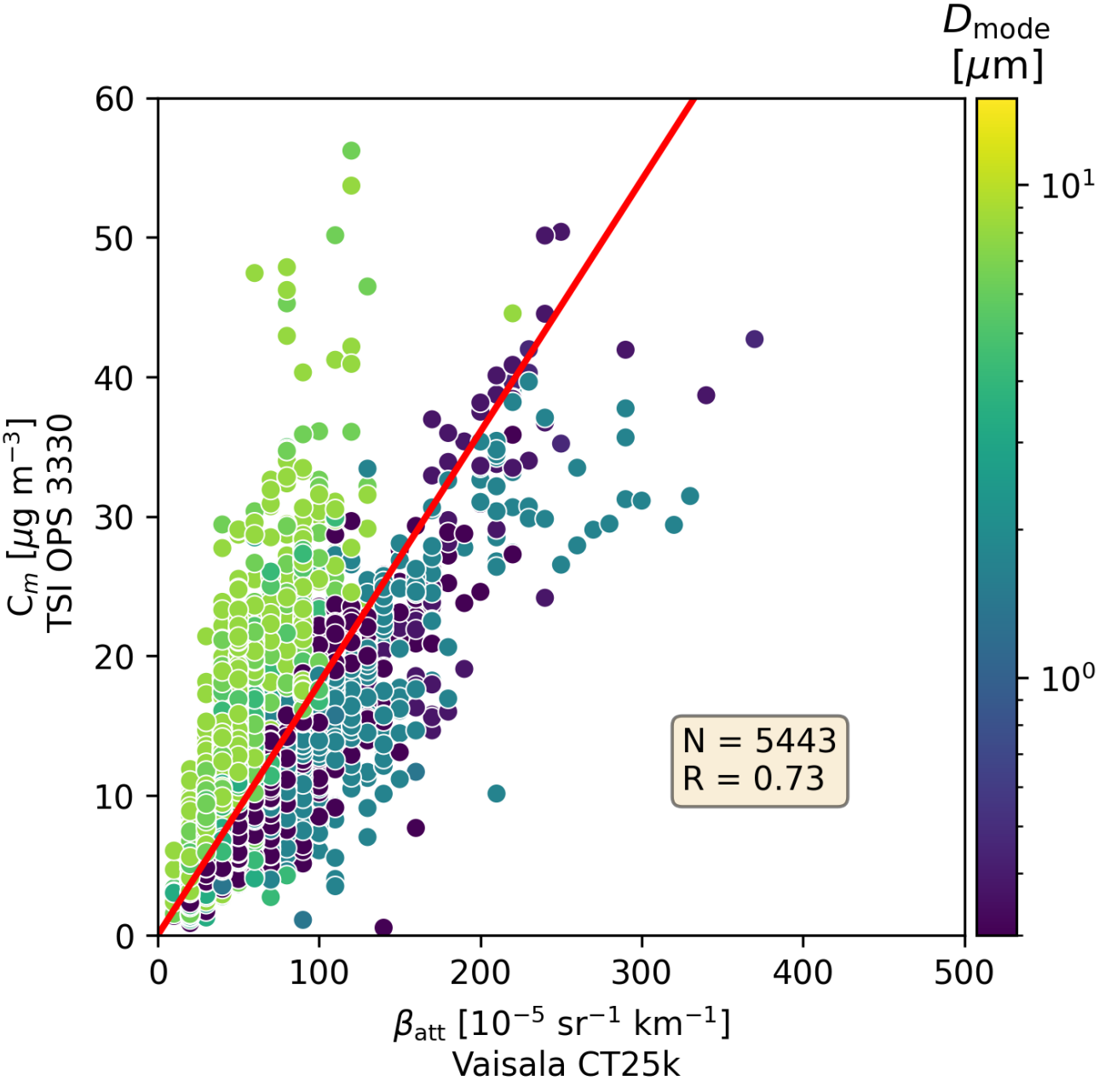

Figure 5. Comparison of ceilometer attenuated backscatter coefficients β_{att} in 120 m and total in situ aerosol mass concentration C_{m} (01 February - 20 June 2023). The inset indicates the number of data points N and the correlation coefficient R. The full red line shows the result of a linear regression (Eq. 12). Data points were color-coded according to the diameter D_{mode} of the size bin with the maximum aerosol mass concentration.

https://doi.org/10.5194/egusphere-2026-131
Preprint. Discussion started: 19 January 2026

For the following analyses, a combined dataset based on OPS-measurement, ceilometer, and Cloudnet data was generated. All data were mapped on the 5-minute time grid of the OPS-measurements based on a nearest neighbour approach, resulting in a total of 5443 data points after applying the filtering criteria (Sec. 5.1). Figure 5 indicates a linear correlation between ceilometer attenuated backscatter coefficient β_{att} and in situ aerosol mass concentration C_{m} with a Pearson correlation coefficient R = 0.73. This result is in reasonable agreement with a previous study by Münkel et al. (2006) who obtained a correlation coefficient of R = 0.84 between ground-level PM10 aerosol mass concentration and the attenuated backscatter coefficient of a co-located CT25k in an urban environment.

To derive an empirical relationship between attenuated backscatter coefficients and total aerosol mass concentrations, a least squares linear regression was derived resulting in the following expression for a ceilometer-derived aerosol mass concentration C_{m}^{β}:

$$\frac{C_{\mathrm{m}}^{\beta}}{\mu\mathrm{g\ m^{-3}}} = 0.18 \cdot \frac{\beta_{\mathrm{att}}}{10^{-5}\mathrm{sr^{-1}km^{-1}}} \tag{12}$$

Neglecting the small contribution of molecular backscatter that is discussed in Sect. 5.3, the line was forced through the origin. The corresponding regression line is shown in Fig. 5. Its slope is again in reasonable agreement with the result by Münkel et al. (2006) who derived a value of 0.20×10^{5} μg m^{-3} sr km and a small offset of -1.6 μg m^{-3}.

To estimate the uncertainty of deriving aerosol mass concentration from β_{att}, a mean absolute percentage error (MAPE) was calculated considering all N data points:

$$\Delta C_{\mathrm{m}}^{\beta} = \frac{1}{N}\sum_{i=1}^{N}\left|\frac{C_{\mathrm{m},i}^{\beta} - C_{\mathrm{m},i}}{C_{\mathrm{m},i}}\right| \times 100\ \% = 31\ \% \tag{13}$$

The corresponding RMSE is 4.7 μg m^{-3}. As is evident from Fig. 5 the scatter is significant and can be explained by instrumental uncertainties, varying aerosol optical properties, aerosol composition, particle size, and particle shape. The color-coding based on the diameter D_{mode} of the OPS size bin with the maximum aerosol mass concentration implies a dependence of the relationship on the particle size distribution that is addressed in Sect. 5.4.

This analysis demonstrates that ceilometer β_{att} measurements are, in principle, suitable for obtaining information on aerosol mass concentration. However, the statistical relation obtained here is valid only for the site- and instrument-specific set-up.

5.3 Aerosol mass concentration and extinction coefficient

In this section we now analyse the relation of the in situ measured aerosol mass concentrations to the aerosol extinction coefficients, derived from β_{att}. Any influence of molecular backscatter that is included in β_{att} should be eliminated in the retrieval of aerosol extinction coefficients. Ceilometer-derived σ_{a} were calculated from the ceilometer attenuated backscatter coefficient β_{att} by the forward inversion method described in Sec. 4.2 (Li et al., 2021). Figure 6 shows the obtained σ_{a} as a function of the corresponding β_{att} revealing a compact linear relationship with a correlation coefficient close to unity. A linear regression results in:

https://doi.org/10.5194/egusphere-2026-131
Preprint. Discussion started: 19 January 2026

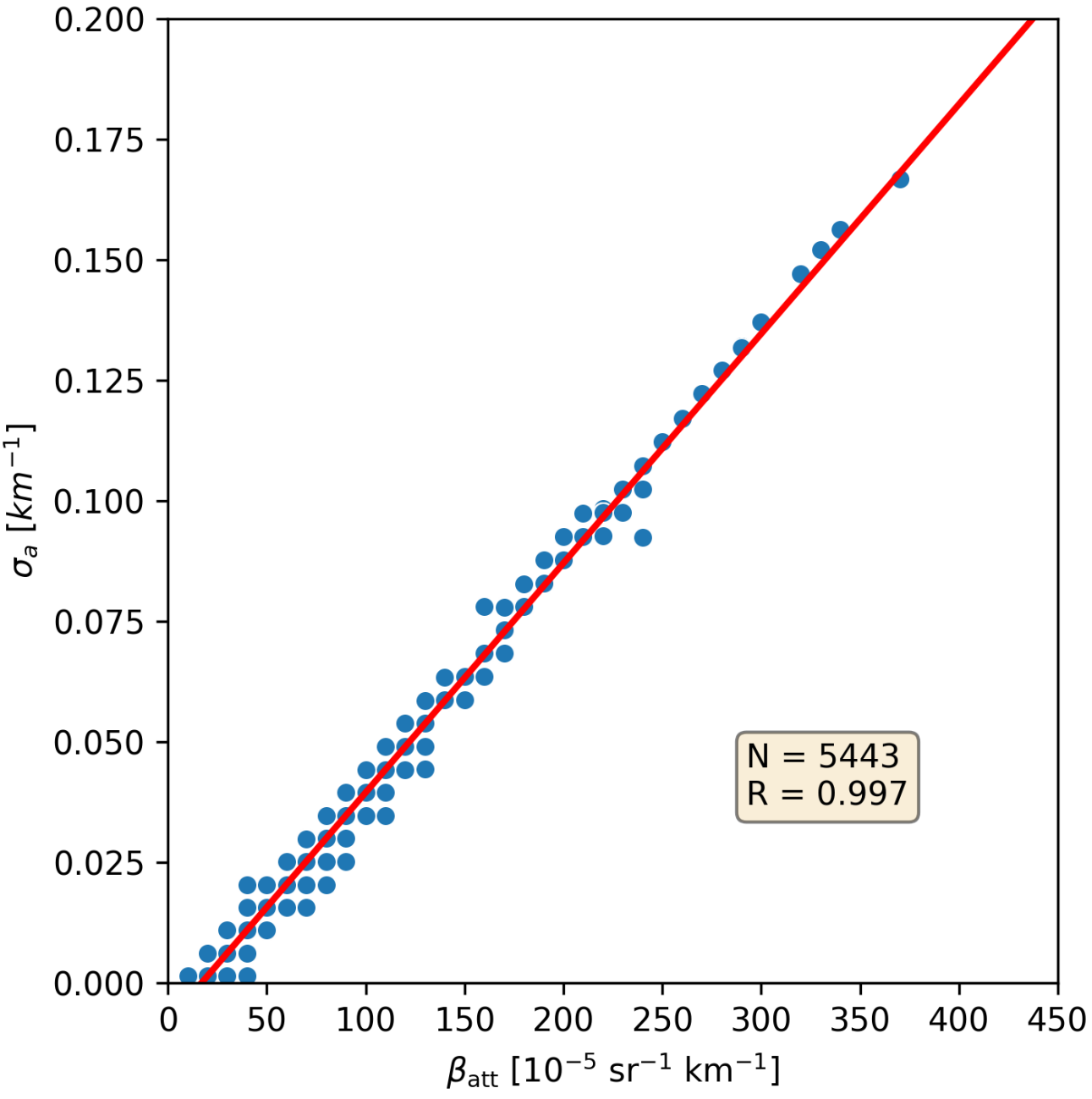

Figure 6. Comparison of ceilometer attenuated backscatter coefficients β_{att} in 120 m and corresponding aerosol extinction coefficients σ_{a}, derived by a forward inversion method (01 February - 20 June 2023) according to Li et al. (2021). The inset indicates the number of data points N and the correlation coefficient R. The red line corresponds to the regression line (Eq. 14).

https://doi.org/10.5194/egusphere-2026-131
Preprint. Discussion started: 19 January 2026

$$\frac{\sigma_{\mathrm{a}}}{\mathrm{km}^{-1}} = -0.008 + 47.6 \cdot \frac{\beta_{\mathrm{att}}}{\mathrm{sr}^{-1}\mathrm{km}^{-1}} \tag{14}$$

The slope of 47.6 sr closely resembles the a priori lidar ratio of $S_{\mathrm{a}} = 47$ sr that was applied (Sec. 4.2) with a y-intercept of -0.008 km^{-1}. This intercept corresponds to the influence of molecular backscatter that is included in β_{att} and should be eliminated in the retrieval of σ_a. The intercept value can be converted to a pure air backscattering coefficient of 1.7×10^{-4} sr^{-1}km^{-1}. Taking the theoretical Rayleigh scattering lidar ratio of $8\pi/3$ sr, an extinction coefficient of 1.4×10^{-3} km^{-1} at 120 m was derived. This value is in reasonable agreement with a literature value of 1.53×10^{-3} km^{-1} for 906 nm (Bucholtz, 1995).

Because of the strong correlation between β_{att} and σ_{a}, a plot of C_{m} as a function of σ_{a} exhibits virtually the same scatter as C_{m} as a function of β_{att} (Fig. 5) with a similar Pearson correlation coefficient of R = 0.73. The corresponding plot is shown in Fig. 7.

https://doi.org/10.5194/egusphere-2026-131
Preprint. Discussion started: 19 January 2026

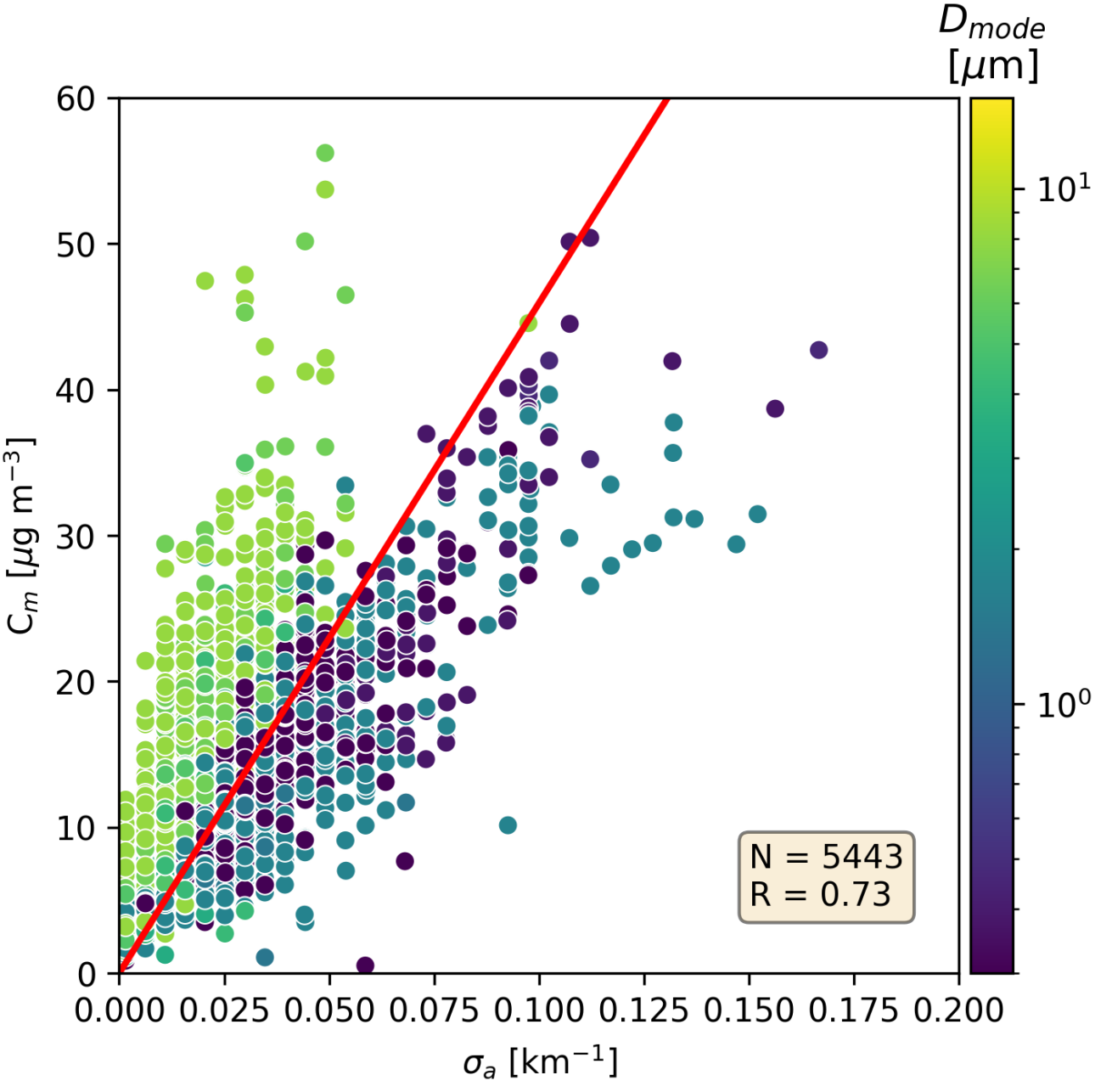

Figure 7. Comparison of ceilometer-derived aerosol extinction coefficients σ_{a} in 120 m and total in situ aerosol mass concentration C_{m} (01 February - 20 June 2023). The inset indicates the number of data points N and the correlation coefficient R. The full red line shows the result of a linear regression (Eq. 15). Data points were color-coded according to the diameter D_{mode} of the size bin with the maximum aerosol mass concentration.

https://doi.org/10.5194/egusphere-2026-131
Preprint. Discussion started: 19 January 2026

A linear regression through the origin between C_m and σ_a results in an empirical relation for an extinction-derived aerosol mass concentration C_m^σ:

$$\frac{C_\mathrm{m}^\sigma}{\mu\mathrm{g\ m^{-3}}} = 460 \cdot \frac{\sigma_\mathrm{a}}{\mathrm{km^{-1}}} \tag{15}$$

Consistently, no improvement in the relative uncertainty of deriving aerosol mass concentration from σ_a was achieved, i.e. $\Delta C_\mathrm{m}^\sigma$ = 39 % (RSME = 5.7 μg m^{-3}), compared to $\Delta C_\mathrm{m}^\beta$ = 31 %. However, knowledge of the true lidar ratio for each measurement is expected to reduce $\Delta C_\mathrm{m}^\sigma$, making σ_a a better proxy for the aerosol mass concentration. This hypothesis is discussed in the next section.

Equation 15 corresponds to EMC= $(2.2 \pm 0.9)\ \mathrm{m^2 g^{-1}}$, which is high compared to literature values from ceilometer networks like ALICEnet: EMC = (0.9–1.2) $\mathrm{m^2 g^{-1}}$ and UK Met Office: EMC = (0.7–1.3) $\mathrm{m^2 g^{-1}}$ (Osborne et al., 2024). Part of this difference can be explained by the smaller wavelength of the Vaisala CT25k (906 nm) compared to the Lufft CHM15k (1064 nm) for which the literature values apply. Typical Angström exponents of 1.2±0.5 would result in ratios $\sigma_{\mathrm{a},1064}/\sigma_{\mathrm{a},906} = 0.83 \pm 0.06$ shifting the EMC closer to the literature values, i.e. EMC= $(1.8 \pm 0.7)\ \mathrm{m^2 g^{-1}}$ for a wavelength of 1064 nm.

5.4 Calculation of aerosol backscatter and extinction coefficients

In this section, we now attempt to explain the discrepancies in the derived EMC to previous literature studies. For this, we simulated β_a and σ_a based on Mie-theory and the measured OPS size distributions. Following an approach by Sundström et al. (2009), particle extinction efficiencies Q_ext for the ceilometer wavelength of λ = 906 nm were calculated (Prahl, 2025) for 1000 spherical aerosol particles with diameters linearly distributed between 0.3 and 10 μm. Refractive indices were varied between m = 1.3−0i (water) and m = 1.7−0i (dolomite), covering a typical range of naturally occurring particle properties (Reid et al., 2003). For each size bin of the OPS (Tab. A1), the mean of Q_ext was calculated and converted to the aerosol extinction cross section by multiplication with the geometrical cross section $\pi D_\mathrm{pv}^2/4$. The total aerosol extinction coefficients $\sigma_\mathrm{a}^\mathrm{Mie}$ for each OPS measurement were then calculated based on the measured aerosol number size distribution. Mean size bin lidar ratios were determined accordingly from the phase functions of the spherical particles. Combined with the extinction coefficients, aerosol backscatter coefficients were obtained for the size bins and finally the $\beta_\mathrm{a}^\mathrm{Mie}$ of the measured size distributions. The different ranges of $\beta_\mathrm{a}^\mathrm{Mie}$ for the different refractive indices are shown in Fig. 8. Lidar ratios $S_\mathrm{a}^\mathrm{Mie} = \sigma_\mathrm{a}^\mathrm{Mie}/\beta_\mathrm{a}^\mathrm{Mie}$ for the size distributions can be defined as well.

https://doi.org/10.5194/egusphere-2026-131
Preprint. Discussion started: 19 January 2026

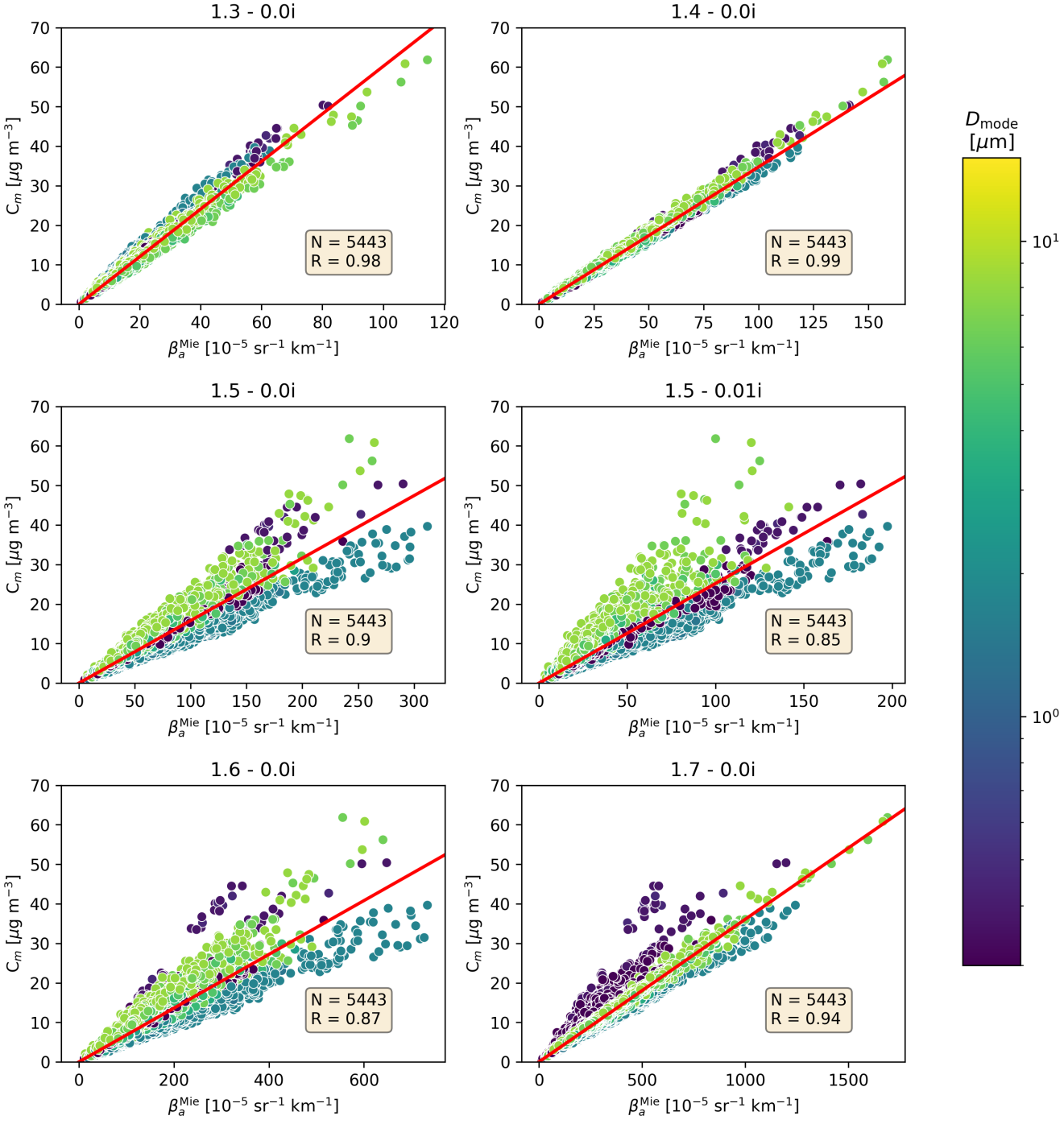

Figure 8. Comparison of simulated aerosol backscatter coefficients β_a^{Mie} for different refractive indices, based on in situ aerosol size distributions in 120 m and total in situ aerosol mass concentration C_{m} (01 February - 20 June 2023). The inset indicates the number of data points N and the correlation coefficient R. The full red line shows the result of a linear regression (Tab. 3). Data points were color-coded according to the diameter D_{mode} of the size bin with the maximum aerosol mass concentration.

https://doi.org/10.5194/egusphere-2026-131
Preprint. Discussion started: 19 January 2026

The results of the calculations are summarized in Tab. 3. Slopes and correlation coefficients of regression lines for different particle refractive indices are listed for C_{m} as a function of $\sigma_{\mathrm{a}}^{\mathrm{Mie}}$ and $\beta_{\mathrm{a}}^{\mathrm{Mie}}$, $\sigma_{\mathrm{a}}^{\mathrm{Mie}}$ as a function of σ_{a}, as well as the lidar ratios $S_{\mathrm{a}}^{\mathrm{Mie}}$ for the 5443 size distributions. With one exception, correlation coefficients range above 0.82.

https://doi.org/10.5194/egusphere-2026-131
Preprint. Discussion started: 19 January 2026

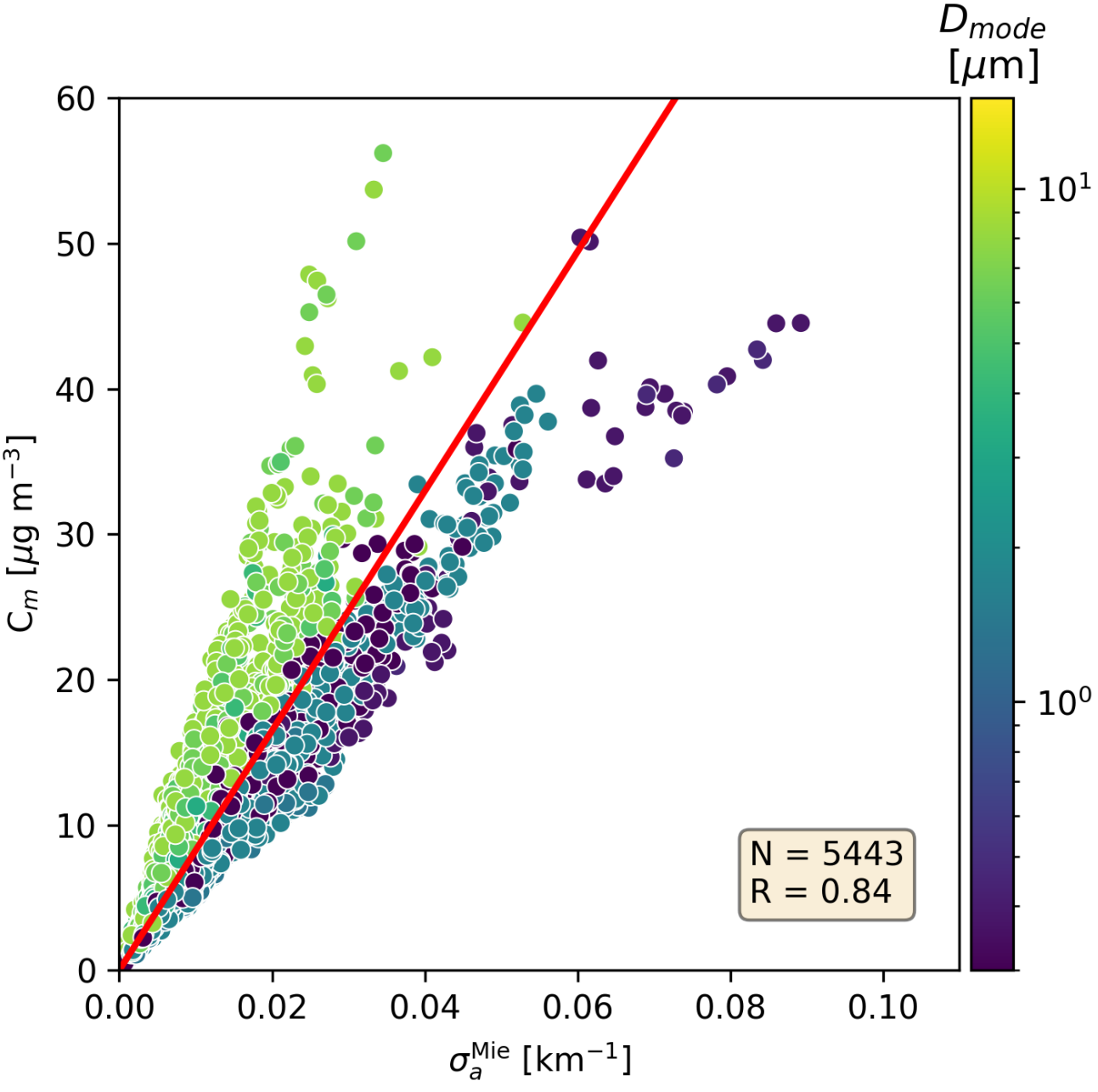

Figure 9. Comparison of simulated aerosol extinction coefficients σ_a^{Mie} for a refractive index of 1.5, based on in situ aerosol size distributions in 120 m and total in situ aerosol mass concentration C_{m} (01 February - 20 June 2023). The inset indicates the number of data points N and the correlation coefficient R. The full red line shows the result of a linear regression (Tab. 3). Data points were color-coded according to the diameter D_{mode} of the size bin with the maximum aerosol mass concentration.

https://doi.org/10.5194/egusphere-2026-131
Preprint. Discussion started: 19 January 2026

As an example, Fig. 9 shows the dependence of measured C_{m} as a function of $\sigma_{\mathrm{a}}^{\mathrm{Mie}}$ for a refractive index of 1.5, revealing a comparable scatter and color-coding pattern as in Figs. 5 and 7. A plot of calculated and ceilometer-derived extinction coefficients against each other is shown for this example in Fig. 10 and confirms that the D_{mode} dependence no longer affects the relationship, which is reflected in a greater correlation coefficient of R = 0.92 compared to R = 0.73 in Figs. 5 and 7, and R = 0.84 in Fig. 9. This result can be explained by different particle size dependencies of the aerosol particle mass ($\propto D^3$) and scattering cross section ($\propto D^2$) which adversely affect the correlations of aerosol mass concentrations and extinction coefficients for the investigated collection of variable size distributions. However, despite the strong correlation in Fig. 10, the $\sigma_{\mathrm{a}}^{\mathrm{Mie}}$ and σ_{a} differ by a factor of about 0.5. Comparable results were obtained for other refractive indices which produce ratios between $\sigma_{a}^{\mathrm{Mie}}$ and σ_{a} in a reasonably narrow range of 0.49±0.17 (Tab. 3).

In contrast, the C_{m} to $\beta_{\mathrm{a}}^{\mathrm{Mie}}$ relationships and the $S_{\mathrm{a}}^{\mathrm{Mie}}$ exhibt a much greater variation, compared to the C_{m} to $\sigma_{a}^{\mathrm{Mie}}$ relationships because of strongly increasing backscattering efficiencies with increasing refractive index (Tab. 3). In addition, as already shown by Sundström et al. (2009), for spherical particles in the size range 1–10 μm strong variations and distinct maxima in the phase function in backscattering direction exist, i.e. minima in the lidar ratios. On the other hand, Sundström et al. (2009) demonstrated that these minima do not occur for non-spherical particles which can explain the overall smaller $S_{\mathrm{a}}^{\mathrm{Mie}}$ compared to the AERONET based value of 47 sr used in the retrieval (Sect. 4.2). Note that lidar ratios in a range 40–50 sr are applied in the aformentione ceilometer networks (Osborne et al., 2024) in agreement with the value used in this work. However, a column-mean lidar ratio might not be representative of the boundary layer. Nevertheless, the theoretical calculations summarized in Tab. 3 confirm that empirical, linear relationsships between C_{m} and σ_{a} are robust with regard to variations of refractive indices in the particle phase. Moreover, the resulting EMC = $1/r_3$ (Tab. 3) of (1.3 ± 0.4) $\mathrm{m^2 g^{-1}}$ are in the range of the literature values.

refractive index	$\sigma_{\mathrm{a}}^{\mathrm{Mie}} = r_1 \times \sigma_{\mathrm{a}}$		$C_{\mathrm{m}} = r_2 \times \beta_{\mathrm{a}}^{\mathrm{Mie}}$		$C_{\mathrm{m}} = r_3 \times \sigma_{\mathrm{a}}^{\mathrm{Mie}}$		$S_{\mathrm{a}}^{\mathrm{Mie}}$
	r_1	R	r_2	R	r_3	R	
	[km km^{-1}]		[10^5 μg m^{-3} sr km]		[μg m^{-3} km]		[sr]
1.3 − 0i	0.32	0.86	0.60	0.98	1100	0.86	53±20
1.4 − 0i	0.40	0.90	0.35	0.99	920	0.85	35±9
1.5 − 0i	0.47	0.92	0.16	0.90	820	0.84	17±4
1.5 − 0.01i	0.43	0.92	0.25	0.85	900	0.82	25±4
1.6 − 0i	0.55	0.90	0.068	0.87	710	0.82	7.8±3.3
1.7 − 0i	0.65	0.88	0.036	0.94	606	0.78	4.6±2.9

Table 3. Slopes of regression lines (r) and Pearson correlation coefficients (R) of the relationships between simulated aerosol properties based on measured size distributions ($\sigma_{\mathrm{a}}^{\mathrm{Mie}}$, $\beta_{\mathrm{a}}^{\mathrm{Mie}}$), ceilometer-derived extinction coefficients (σ_{a}) and in situ measured aerosol mass concentration (C_{m}) as a function of particle refractive index. The last column contains the simulated lidar ratio $S_{\mathrm{a}}^{\mathrm{Mie}}$.

https://doi.org/10.5194/egusphere-2026-131
Preprint. Discussion started: 19 January 2026

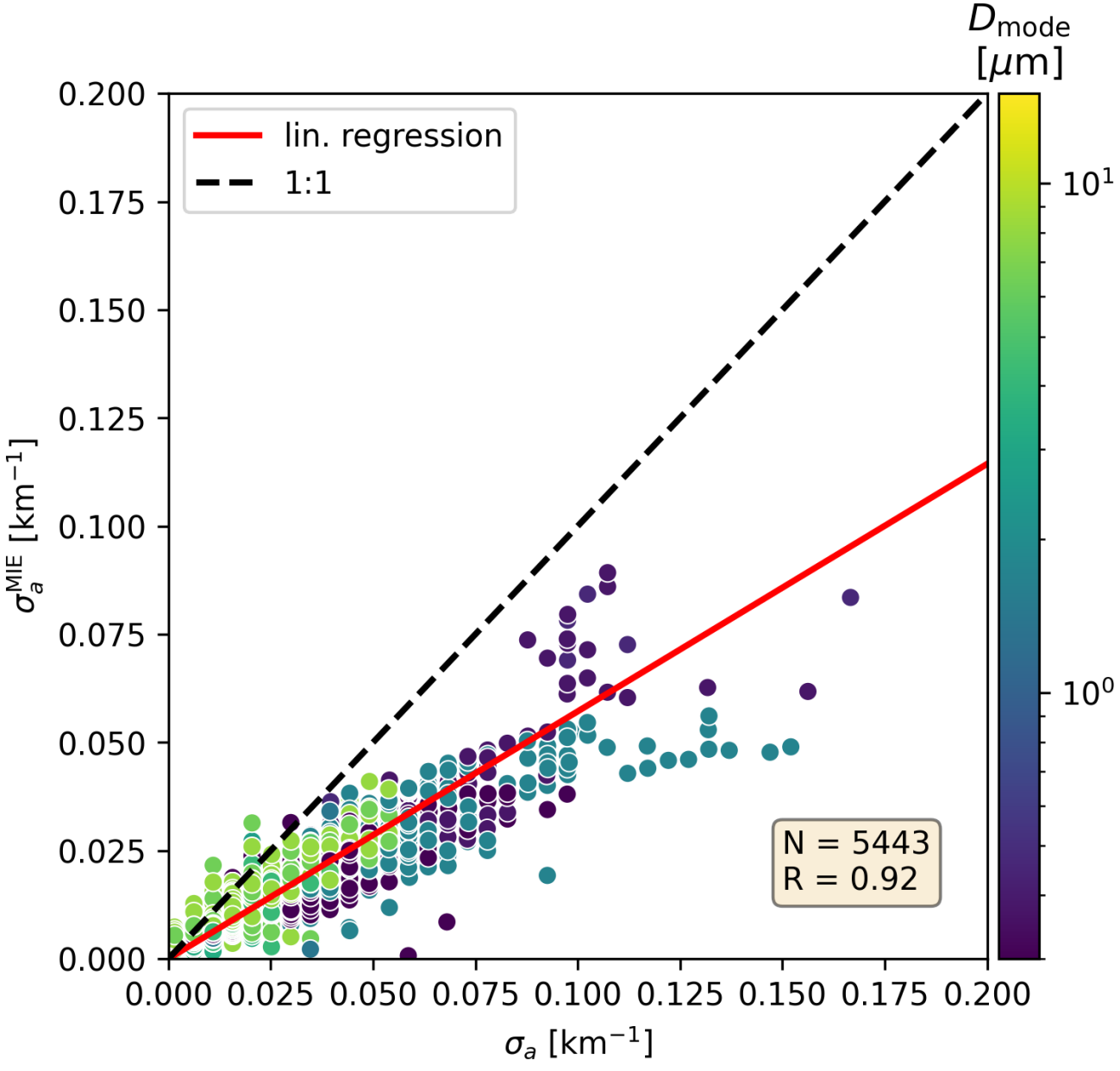

Figure 10. Comparison of ceilometer-derived aerosol extinction coefficients σ_{a} in 120 m and simulated aerosol extinction coefficients σ_a^{Mie} based on in situ aerosol size distributions (01 February - 20 June 2023) for an refractive index of 1.5−0i. The inset indicates the number of data points N and the correlation coefficient R. The full red line shows the result of a linear regression. Data points were color-coded according to the diameter D_{mode} of the size bin with the maximum aerosol mass concentration.

https://doi.org/10.5194/egusphere-2026-131
Preprint. Discussion started: 19 January 2026

5.5 Size distributions and potential OPS artefacts

The Mie-theory calculations of the previous section rely on accurately determined size distributions from the OPS measurements. The uncertainties of these measurements are challenging to estimate and are not provided by the manufacturer. But major systematic errors are unlikely relying on careful characterisations by the manufacturer. However, the size range that is covered by the OPS is limited to 0.3–10 μm. The influence of particles greater than 10 μm is uncertain. They are probably correctly discarded because of scattered light signals that are too high. On the other hand, such particels will contribute to the scattered light received by the ceilometer. Similarly, particles smaller than 0.3 μm are not registered because they produce too small signals, but their contribution to the backscatter may still be significant. In addition, particles may be lost in the upstream inlet system before they can enter the OPS. These limitations have in common that they decrease the registered number and mass concentrations of particles that are nonetheless present and potentially relevant for the ceilometer measurements. Without a full characterisation of the size distribution beyond the size range of the OPS, a quantification of the missed aerosol mass concentration and the corresponding simulated aerosol extinction is not meaningful.

https://doi.org/10.5194/egusphere-2026-131
Preprint. Discussion started: 19 January 2026

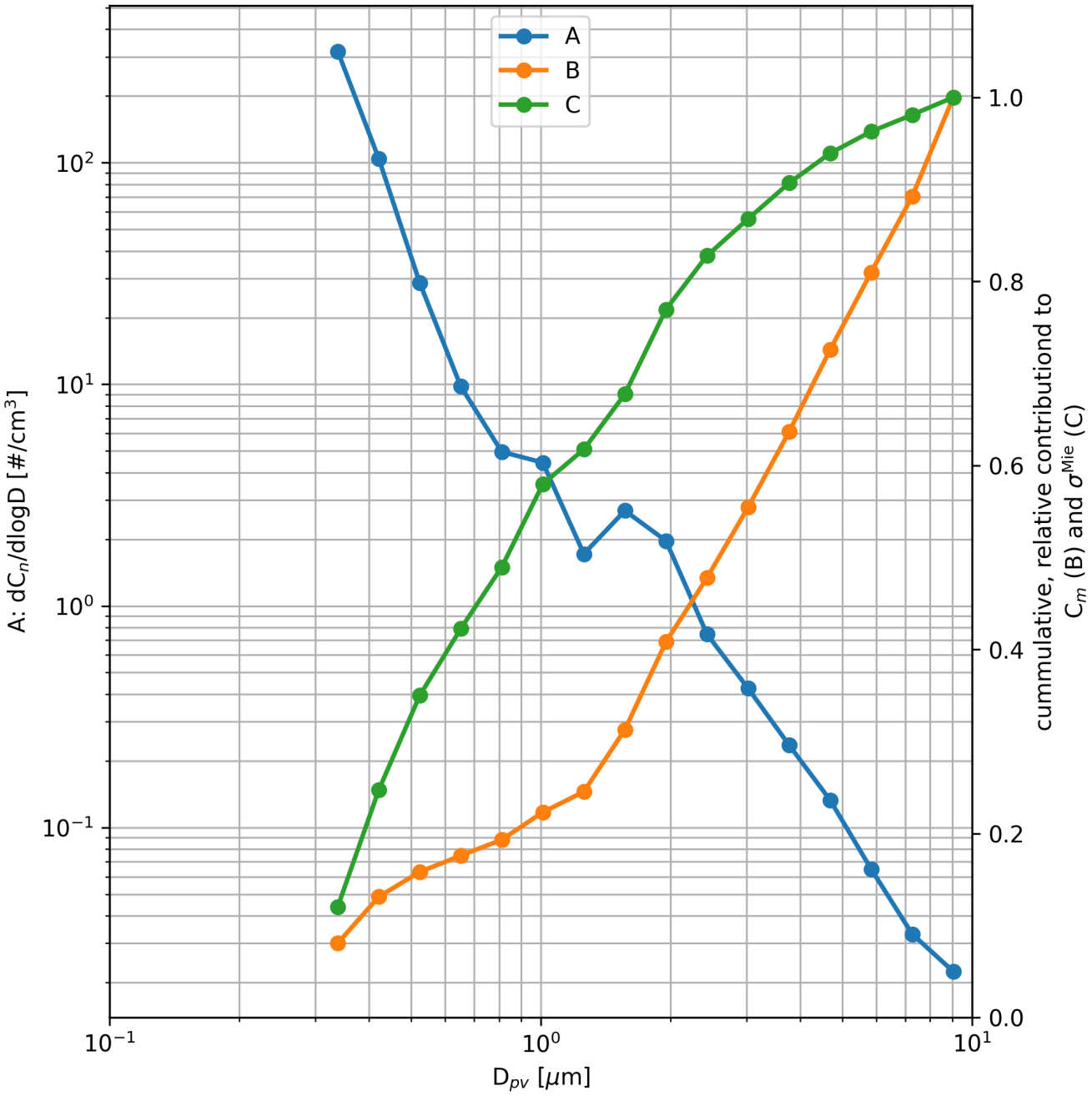

Figure 11. Mean aerosol number size distribution $\mathrm{d}C_\mathrm{n}/\mathrm{d}\log D$ (A), cumulative, relative contribution to total aerosol mass concentration C_m (B) and to simulated aerosol extinction coefficients $\sigma_\mathrm{a}^\mathrm{Mie}$ (C) (01 February to 20 June 2023 at the meteorological tower in 120 m).

https://doi.org/10.5194/egusphere-2026-131
Preprint. Discussion started: 19 January 2026

To illustrate the problem, Fig. 11 depicts the full measurement period's mean aerosol size distribution of this work showing the typical increase of number concentrations towards smaller particle diameters which can be expected to continue to diameters below 0.3 μm and greater than 10 μm. On the right hand axis, the cumulative, relative contributions of the size bins to the measured total aerosol mass concentration C_{m} and the simulated aerosol extinction coefficient $\sigma_{\mathrm{a}}^{\mathrm{Mie}}$ for a refractive index of 1.5 are shown on a linear scale for comparison. The extinction coefficient increase towards the greatest D_{pv} is already levelling out. The contribution of particles greater than 10 μm is therefore assumed to be limited. On the other hand, the contributions of the size bin with the smallest D_{pv} are already on the order of 10% for both aerosol mass concentration and aerosol extinction coefficient. It is therefore plausible that particles with diameters < 0.3 μm have contributed substantially to the ceilometer backscatter and the retrieved extinction coefficients. This could qualitatively explain why the EMC obtained in this work is greater than those in literature and those derived from Mie theory. For the latter the size range limitations seem to be less significant because of compensating effects, i.e. by missing aerosol mass concentration and missing aerosol extinction. Fig. 11 also illustrates the apparent D_{mode} dependence of the σ_a vs. C_{m} relationships in Figs. 6 and 7. An elevated contribution of particels with $D_{\mathrm{pv}} < 1$ μm would increase the $\sigma_{\mathrm{a}}^{\mathrm{Mie}}$ more strongly than C_{m} while for particels with $D_{\mathrm{pv}} > 2$ μm the opposite is the case: the C_{m} increase would exceed that of $\sigma_{\mathrm{a}}^{\mathrm{Mie}}$.

6 Conclusion

In this study, we assessed different aerosol properties derived from a Vaisala CT25k ceilometer, aiming to evaluate the potential of an existing multi-year ceilometer dataset at the Jülich Observatory for Cloud Evolution (JOYCE) for aerosol remote sensing. The calibration of the ceilometer signal was verified with a liquid cloud calibration (Hopkin et al., 2019). The attenuated backscatter signal was then used to derive aerosol extinction coefficients with a forward inversion method (Li et al., 2021; Mortier, 2022). All tools used in this study are available and can be easily transferred to other ceilometers and ALC networks.

To evaluate the uncertainty of the forward inversion method, an in situ comparison measurement was set up by installing an optical particle sizer (OPS) at 120 m above ground on a meteorological tower in Jülich. This allowed us to measure aerosol size distributions in a range 0.3–10 μm. From the vertical ceilometer profiles, we selected data close to 120 m and compared them to the in situ measurements. A 120-day dataset between 01 February and 20 June 2023 covered by both instruments was analysed. The Cloudnet (Illingworth et al., 2007) target classification was used in combination with a limit in radar reflectivity and relative humidity to exclude the presence of hydrometeors.

In situ aerosol mass concentration C_{m} was correlated to ceilometer-based attenuated backscatter β_{att} and aerosol extinction σ_{a} coefficients with a Pearson correlation coefficient of $R = 0.73$ for both. Ordinary least square fits resulted in empirical conversion coefficients of 0.18×10^5 μg m^{-3} sr km and 460 μg m^{-3} km for β_{att} and σ_{a} respectively. The uncertainties of these conversions were quantified by mean absolute percentage errors of 31% (β_{att}) and 39% (σ_{a}). However, the σ_{a} to C_{m} conversion factor, which corresponds to the inverse of an extinction-to-mass coefficient of (2.2 ± 0.9) m^{2}g^{-1}, is greater by a facor of about 1.8 compared to the literature values (Osborne et al., 2024). To gain further insight into the role of size distributions and the refractive index on the retrievals, Mie calculations were performed based on in situ measurements. These revealed

https://doi.org/10.5194/egusphere-2026-131
Preprint. Discussion started: 19 January 2026

that σ_{a} only weakly depends on the refractive index in comparison to the aerosol backscatter coefficients β_{a}. The $\sigma_{\mathrm{a}}^{\mathrm{Mie}}$ to C_{m} conversion factors based on the Mie calculations were found to be in reasonable agreement with literature values, also indicating a systematic underestimation of the ceilometer-derived conversion factor σ_a to C_{m}. This disagreement is qualitatively explainable by the limited detection range of the OPS that excludes small particles (< 0.3 μm) that may contribute significantly the ceilometer signal.

This study confirmed that the retrieval (Mortier, 2022; Li et al., 2021) of σ_{a} from β_{att} is viable based on accurate lidar ratios, justifying the use of existing ceilometer datasets. However, the conversion from σ_a to C_m can introduce significant uncertainties. Moreover, the instrument used here (Vaisala CT25k) does not represent the performance of modern ceilometers. It is recommended to reevalute the approach with state-of-the-art instrumentation for future applications.

Code and data availability. The code used in this study and references to all utilised datasets were published at: Müller, Marcus G.; Bohn, Birger; Löhnert, Ulrich, 2025, "Code and Data for Uncertainty estimation of ceilometer aerosol properties", https://doi.org/10.26165/JUELICH-DATA/EMCX36, Jülich DATA

https://doi.org/10.5194/egusphere-2026-131
Preprint. Discussion started: 19 January 2026

Appendix A

Table A1. OPS bin lower limits D_{L}, upper limits D_{U} and effective diameters D_{pv} in μm.

Bin	D_{L}	D_{U}	D_{pv}
1	0.30	0.37	0.34
2	0.37	0.47	0.42
3	0.47	0.58	0.52
4	0.58	0.72	0.65
5	0.72	0.90	0.81
6	0.90	1.12	1.01
7	1.12	1.39	1.26
8	1.39	1.73	1.57
9	1.73	2.16	1.95
10	2.16	2.69	2.43
11	2.69	3.34	3.03
12	3.34	4.16	3.77
13	4.16	5.18	4.69
14	5.18	6.45	5.84
15	6.45	8.03	7.27
16	8.03	10.00	9.05

Author contributions. All co-authors contributed to the development of the work. The study was performed by MM within the framework of his PhD, supervised by BB and UL. The original draft was created by MM. BB and UL contributed to review and editing.

Competing interests. The authors declare, that none of the authors have any competing interests.

Acknowledgements. We thank Patrizia Ney (Forschungszentrum Jülich) and colleagues for the opportunity to perform in situ measurements at the Jülich meteorological tower and for providing technical support. We thank E-Profile for granting access to the ceilometer proccessing code. We acknowledge ACTRIS and the Finnish Meteorological Institute for providing Cloudnet data. We thank the AERONET project for providing data products based on the FZJ-JOYCE sun photometer.

https://doi.org/10.5194/egusphere-2026-131
Preprint. Discussion started: 19 January 2026

References

Ackerman, A. S., Toon, O. B., Stevens, D. E., Heymsfield, A. J., Ramanathan, V., and Welton, E. J.: Reduction of Tropical Cloudiness by Soot, Science, 288, 1042–1047, https://doi.org/10.1126/science.288.5468.1042, 2000.

Albrecht, B. A.: Aerosols, Cloud Microphysics, and Fractional Cloudiness, Science, 245, 1227–1230, https://doi.org/10.1126/science.245.4923.1227, 1989.

Bucholtz, A.: Rayleigh-scattering calculations for the terrestrial atmosphere, Applied Optics, 34, 2765–2773, https://doi.org/10.1364/AO.34.002765, publisher: Optica Publishing Group, 1995.

Cloudnet: Cloudnet sites, https://cloudnet.fmi.fi/sites, 2025.

D'Amico, G., Amodeo, A., Baars, H., Binietoglou, I., Freudenthaler, V., Mattis, I., Wandinger, U., and Pappalardo, G.: EARLINET Single Calculus Chain - overview on methodology and strategy, Atmospheric Measurement Techniques, 8, 4891–4916, https://doi.org/10.5194/amt-8-4891-2015, 2015.

E-Profile: Metadata - Ceilometers, https://e-profile.eu/metadata, last access: 22 August 2025, 2025.

Eckert, R.: Inbetriebnahme und Optimierung eines Messsystems zur Partikelgrößenmessung in der Atmosphäre, Ph.D. thesis, FH Aachen, 2013.

Haefele, A., Hervo, M., Turp, M., Lampin, J.-L., Haeffelin, M., and Lehmann, V.: The E-PROFILE network for the operational measurement of wind and aerosol profiles over Europe the E-PROFILE team, and the TOPROF team, 2016.

Hervo, M., Poltera, Y., and Haefele, A.: An empirical method to correct for temperature-dependent variations in the overlap function of CHM15k ceilometers, Atmospheric Measurement Techniques, 9, 2947–2959, https://doi.org/10.5194/amt-9-2947-2016, publisher: Copernicus GmbH, 2016.

Hogan, R. J. and O'Connor, E. J.: Facilitating cloud radar and lidar algorithms: the Cloudnet Instrument Synergy/Target Categorization product, 2004.

Holben, B. N., Eck, T. F., Slutsker, I., Tanré, D., Buis, J. P., Setzer, A., Vermote, E., Reagan, J. A., Kaufman, Y. J., Nakajima, T., Lavenu, F., Jankowiak, I., and Smirnov, A.: AERONET-A Federated Instrument Network and Data Archive for Aerosol Characterization tion of a new Sun-sky scanning radiometer system that, ENVIRON, 66, 1–16, http://spamer.gsfc.nasa.gov., 1998.

Hopkin, E., Illingworth, A. J., Charlton-Perez, C., Westbrook, C. D., and Ballard, S.: A robust automated technique for operational calibration of ceilometers using the integrated backscatter from totally attenuating liquid clouds, Atmospheric Measurement Techniques, 12, 4131–4147, https://doi.org/10.5194/amt-12-4131-2019, publisher: Copernicus GmbH, 2019.

Illingworth, A. J., Hogan, R. J., O'Connor, E., Bouniol, D., Brooks, M. E., Delanoé, J., Donovan, D. P., Eastment, J. D., Gaussiat, N., Goddard, J. W. F., Haeffelin, M., Baltink, H. K., Krasnov, O. A., Pelon, J., Piriou, J.-M., Protat, A., Russchenberg, H. W. J., Seifert, A., Tompkins, A. M., van Zadelhoff, G.-J., Vinit, F., Willén, U., Wilson, D. R., and Wrench, C. L.: Cloudnet, Bulletin of the American Meteorological Society, 88, 883–898, https://doi.org/10.1175/BAMS-88-6-883, 2007.

IPCC: Climate Change 2021: The Physical Science Basis. Contribution of Working Group I to the Sixth Assessment Report of the Intergovernmental Panel on Climate Change, vol. In Press, Cambridge University Press, Cambridge, United Kingdom and New York, NY, USA, https://doi.org/10.1017/9781009157896, 2021.

Klett, J. D.: Stable analytical inversion solution for processing lidar returns, Applied Optics, 20, 211, https://doi.org/10.1364/AO.20.000211, 1981.

https://doi.org/10.5194/egusphere-2026-131
Preprint. Discussion started: 19 January 2026

Klett, J. D.: Lidar inversion with variable backscatter/extinction ratios, Applied Optics, 24, 1638, https://doi.org/10.1364/AO.24.001638, 1985.

Laj, P., Myhre, C. L., Riffault, V., Amiridis, V., Fuchs, H., Eleftheriadis, K., Petäjä, T., Salameh, T., Kivekäs, N., Juurola, E., Saponaro, G., Philippin, S., Cornacchia, C., Arboledas, L. A., Baars, H., Claude, A., De Mazière, M., Dils, B., Dufresne, M., Evangeliou, N., Favez, O., Fiebig, M., Haeffelin, M., Herrmann, H., Höhler, K., Illmann, N., Kreuter, A., Ludewig, E., Marinou, E., Möhler, O., Mona, L., Murberg, L. E., Nicolae, D., Novelli, A., O'Connor, E., Ohneiser, K., Altieri, R. M. P., Picquet-Varrault, B., van Pinxteren, D., Pospichal, B., Putaud, J. P., Reimann, S., Siomos, N., Stachlewska, I., Tillmann, R., Voudouri, K. A., Wandinger, U., Wiedensohler, A., Apituley, A., Comerón, A., Gysel-Beer, M., Mihalopoulos, N., Nikolova, N., Pietruczuk, A., Sauvage, S., Sciare, J., Skov, H., Svendby, T., Swietlicki, E., Tonev, D., Vaughan, G., Zdimal, V., Baltensperger, U., Doussin, J. F., Kulmala, M., Pappalardo, G., Sundet, S. S., and Vana, M.: Aerosol, Clouds and Trace Gases Research Infrastructure (ACTRIS): The European Research Infrastructure Supporting Atmospheric Science, Bulletin of the American Meteorological Society, 105, E1098–E1136, https://doi.org/10.1175/BAMS-D-23-0064.1, publisher: American Meteorological Society, 2024.

Li, D., Wu, Y., Gross, B., and Moshary, F.: Capabilities of an Automatic Lidar Ceilometer to Retrieve Aerosol Characteristics within the Planetary Boundary Layer, Remote Sensing, 13, 1–19, https://doi.org/10.3390/rs13183626, 2021.

Liu, L., Hohaus, T., Franke, P., Lange, A. C., Tillmann, R., Fuchs, H., Tan, Z., Rohrer, F., Karydis, V., He, Q., Vardhan, V., Andres, S., Bohn, B., Holland, F., Winter, B., Wedel, S., Novelli, A., Hofzumahaus, A., Wahner, A., and Kiendler-Scharr, A.: Observational evidence reveals the significance of nocturnal chemistry in seasonal secondary organic aerosol formation, npj Climate and Atmospheric Science, 7, https://doi.org/10.1038/s41612-024-00747-6, publisher: Nature Research, 2024.

Löhnert, U., Schween, J. H., Acquistapace, C., Ebell, K., Maahn, M., Barrera-Verdejo, M., Hirsikko, A., Bohn, B., Knaps, A., O'Connor, E., Simmer, C., Wahner, A., and Crewell, S.: JOYCE: Jülich Observatory for Cloud Evolution, Bulletin of the American Meteorological Society, 96, 1157–1174, https://doi.org/10.1175/BAMS-D-14-00105.1, publisher: American Meteorological Society, 2015.

Mortier, A.: A-Profiles, https://doi.org/10.5281/zenodo.7389683, 2022.

Münkel, C., Eresmaa, N., Räsänen, J., and Karppinen, A.: Retrieval of mixing height and dust concentration with lidar ceilometer, Boundary-Layer Meteorology, 124, 117–128, https://doi.org/10.1007/s10546-006-9103-3, 2006.

O'Connor, E. J., Illingworth, A. J., and Hogan, R. J.: A Technique for Autocalibration of Cloud Lidar, Journal of Atmospheric and Oceanic Technology, 21, 777–786, https://doi.org/10.1175/1520-0426(2004)021<0777:ATFAOC>2.0.CO;2, 2004.

Osborne, M., Barnaba, F., Bellini, A., Buxmann, J., Diemoz, H., Hervo, M., Mattis, I., Mortier, A., and Wagner, F.: Comparison of CHM15k extinction and mass products from ALICEnet, A-Profiles and the UK Met Office, 2024.

Pappalardo, G.: ACTRIS Aerosol, Clouds and Trace Gases Research Infrastructure, EPJ Web of Conferences, 176, 09 004, https://doi.org/10.1051/epjconf/201817609004, 2018.

Pinnick, R. G., Jennings, S. G., Chylek, P., Ham, C., and Grandy, W. T.: Backscatter and extinction in water clouds., Journal of Geophysical Research, 88, https://doi.org/10.1029/JC088iC11p06787, 1983.

Prahl, S.: miepython: Pure python calculation of Mie scattering, https://doi.org/10.5281/zenodo.15514362, 2025.

Quaas, J., Boucher, O., and Lohmann, U.: Constraining the total aerosol indirect effect in the LMDZ and ECHAM4 GCMs using MODIS satellite data, Atmospheric Chemistry and Physics, 6, 947–955, https://doi.org/10.5194/acp-6-947-2006, 2006.

Reid, E. A., Reid, J. S., Meier, M. M., Dunlap, M. R., Cliff, S. S., Broumas, A., Perry, K., and Maring, H.: Characterization of African dust transported to Puerto Rico by individual particle and size segregated bulk analysis, Journal of Geophysical Research: Atmospheres, 108, 2002JD002 935, https://doi.org/10.1029/2002JD002935, 2003.

https://doi.org/10.5194/egusphere-2026-131
Preprint. Discussion started: 19 January 2026

Russell, A. G. and Brunekreef, B.: A Focus on Particulate Matter and Health, Environmental Science & Technology, 43, 4620–4625, https://doi.org/10.1021/es9005459, 2009.

Sarna, K. and Russchenberg, H. W.: Ground-based remote sensing scheme for monitoring aerosol-cloud interactions, Atmospheric Measurement Techniques, 9, 1039–1050, https://doi.org/10.5194/amt-9-1039-2016, publisher: Copernicus GmbH, 2016.

Schween, J. H., Hirsikko, A., Löhnert, U., and Crewell, S.: Mixing-layer height retrieval with ceilometer and Doppler lidar: From case studies to long-term assessment, Atmospheric Measurement Techniques, 7, 3685–3704, https://doi.org/10.5194/amt-7-3685-2014, publisher: Copernicus GmbH, 2014.

Sundström, A. M., Nousiainen, T., and Petäjä, T.: On the quantitative low-level aerosol measurements using ceilometer-type lidar, Journal of Atmospheric and Oceanic Technology, 26, 2340–2352, https://doi.org/10.1175/2009JTECHA1252.1, 2009.

TROPOS: EARLINET, https://www.tropos.de/en/research/projects-infrastructures-technology/coordinated-observations-and-networks/earlinet, last access: 22 August 2025, 2025.

Twomey, S.: The Influence of Pollution on the Shortwave Albedo of Clouds, Journal of the Atmospheric Sciences, 34, 1149–1152, https://doi.org/10.1175/1520-0469(1977)034<1149:TIOPOT>2.0.CO;2, 1977.

Wiegner, M. and Geiß, A.: Aerosol profiling with the Jenoptik ceilometer CHM15kx, Atmospheric Measurement Techniques, 5, 1953–1964, https://doi.org/10.5194/amt-5-1953-2012, 2012.